Solid Freeform Fabrication 2019: Proceedings of the 30th Annual International
Solid Freeform Fabrication Symposium – An Additive Manufacturing Conference
Reviewed Paper

Study on the formability, microstructures and mechanical properties of $AlCrCuFeNi_x$ high-entropy alloys prepared by selective laser melting

Shuncun Luo, Zemin Wang*, Xiaoyan Zeng

Wuhan National Laboratory for Optoelectronics, Huazhong University of Science and Technology, Wuhan 430074, PR China

Abstract

Because of easy cracking caused by rapid solidification, fabricating dual-phase high-entropy alloys (DP-HEAs) through selective laser melting (SLM) has hardly been achieved. Here we reasonably design new DP-HEAs specific to SLM according to solid solutions formation criterion and HEA definition. Results show that Ni addition favors the formation of face-centered cubic (FCC) phase and facilitates the transition from columnar to equiaxed grains, thus the formability of $AlCrCuFeNi_x$ ($2.0 \leq x \leq 3.0$) HEAs is improved. The SLMed $AlCrCuFeNi_{3.0}$ HEA exhibits remarkably heterogeneous microstructures, such as modulated nanoscale lamellar or cellular dual-phase structures, and possesses the best combination of the ultimate tensile strength (~ 957 MPa) and ductility (~ 14.3 %). Also, it is discovered that high densities of Cr-enriched nano-precipitates are embedded in the ordered body-centered cubic (B2) phase. Finally, the underlying strengthening mechanisms are analyzed for the SLMed $AlCrCuFeNi_{3.0}$ HEA.

Keywords: High entropy alloy; Selective laser melting; Microstructure; Strength

Introduction

Due to their excellent mechanical properties, high entropy alloys (HEAs), as a new kind of multicomponent alloys containing at least five major elements, have attracted more and more attention from researchers [1,2]. HEAs favor forming simple solid solutions, such as face-centered cubic (FCC), body-centered cubic (BCC) and FCC + BCC, presumably owing to their 'high entropy effect' [1]. Generally, FCC HEAs exhibit excellent ductility but low strength. However, BCC HEAs show a contrary feature. Additionally, it is hard to realize a simultaneous increase of strength and ductility in single-phase HEAs because the lattice distortion induced strengthening and inherent solid solution strengthening are limited [3].

Intriguingly, dual-phase (DP) or multiple-phase HEAs have been reported to possess superior synthetical properties principally arising from the phase metastability induced hardening and precipitation strengthening, which makes it a promising candidate for practical application in engineering [4-6]. Currently, the preparations of HEAs mainly depend on vacuum arc melting or casting [7], imposing high cost and enormous limitation to produce complex geometry shape.

However, selective laser melting (SLM), a high-efficient and economical laser additive manufacturing (AM) technique, can rapidly fabricate metal components with a complex shape through successive deposition of raw powders layer-by-layer [8]. Recent researches suggest that the SLMed HEA parts exhibit nearly full densification and ultra-fine grains owing to rapid cooling rate (10^5~10^7 K/s) and high controllability of processing during SLM. This leads to better performance compared to that fabricated by casting [9]. Unfortunately, possibly due to

* Corresponding author.
E-mail address: zmwang@hust.edu.cn (Z. Wang).

the inhibited formation of soft FCC phase and easy cracking induced by rapid solidification, processing FCC + BCC DP-HEAs through SLM has never been achieved [10,11]. Only SLMed single-phase FCC HEAs with high ductility have been extensively researched, such as FCC FeCoCrNi [12], C-containing FCC FeCoCrNi [13,14], FCC CoCrFeMnNi [15,16] HEAs.

To explore the feasibility of producing DP-HEA with high strength-ductility combination via SLM, the equiatomic AlCrCuFeNi alloy, as a representative SLMed single-phase BCC HEA [10], is switched to the non-equiatomic $AlCrCuFeNi_x$ (x=2.0, 2.5, 2.75, 3.0) system, which exhibits partial transformation from BCC to FCC phase upon the addition of Ni according to the valence electron concentration (VEC) theory [17,18]. The configurational entropy of $AlCrCuFeNi_3$ alloy is ~150% R (R denotes gas constant), and thus conforms well to the HEA definition. Recent studies indicate that the introduction of a 'heterogeneous microstructure' in metals or alloys can further contribute to achieving high strength-ductility combination, thus overcoming the strength-ductility trade-off [19-21]. Yet whether SLMed DP-HEAs also exhibit the heterogeneous microstructural features remains unclear. Little is known about the structure-property relationship for SLMed DP-HEAs. This study aims to examine the feasibility of SLM printing BCC + FCC DP-HEAs, and then disclose its heterogeneous microstructure as well as deformation behavior.

Experimental methods

In this work, argon gas atomized AlCrCuFeNi alloy powders with an average size of ~ 30.3 μm [10], and Ni powders (purity larger than 99.8 wt.%) with a mean size of ~ 32 μm were used as the original materials. Table 1 shows the chemical composition of AlCrCuFeNi powders. Before SLM processing, the two powders were mixed in the ball mill for 12 h to guarantee the homogeneous mixing of AlCrCuFeNi powders and Ni powders. The representative morphology of the mixed $AlCrCuFeNi_3$ powders is shown in Fig. 1.

Table 1. Chemical composition of the raw AlCrCuFeNi alloy powders.

Element	Al	Cr	Cu	Fe	Ni
Wt.%	11.69	19.92	23.78	21.23	23.38
At.%	22.01	19.46	19.00	19.30	20.22

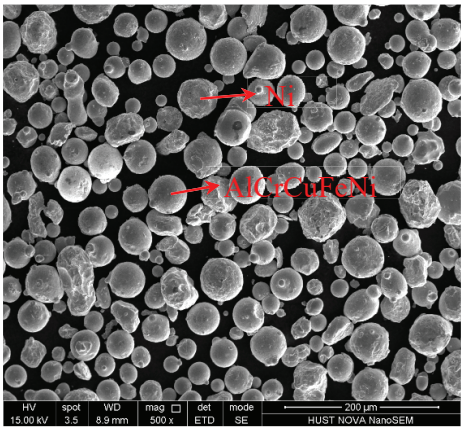

Fig. 1. SEM morphology of the mixed $AlCrCuFeNi_3$ powders.

The SLM experiments were carried out in an argon atmosphere containing < 40 ppm O_2 and H_2O. Simultaneously considering the good formability and high relative density (>99.7%),

the optimal processing parameters for producing $AlCrCuFeNi_x$ (x=2.0, 2.5, 2.75, 3.0) HEAs via SLM were further optimized based on the previous investigation [10], as listed in Table 2.

Phase identification was carried out by using an X-ray diffractometer (XRD, x'pert3 powder) with Cu K_α radiation. The distribution of compositional elements of the as-SLMed sample was analyzed by electron probe microanalysis (EPMA 8050G). A scanning electron microscope (SEM, FEI Gemini SEM 300) equipped with a back-scattered electron (BSE) detector and an electron backscatter diffraction (EBSD) system was applied to observe the microstructures along the building direction. Transmission electron microscopy (TEM) was carried out on Tecnai G2 F30 FEG^{TM} operating at 300 kV. Using the optimal parameters, dog-bone-shaped tensile specimens with the gauge length of 20 mm, the thickness of 1.5 mm and width of 5 mm were printed along the build direction on a self-developed LSNF-1 SLM equipment. Using a Zwick testing machine, uniaxial tension experiments were carried out with a strain rate of 1×10^{-3} s^{-1} at room temperature. To ensure the data reproducibility, three repeated tests were performed.

Table 2. Optimized SLM processing parameters for preparing $AlCrCuFeNi_x$ (x=2.0, 2.5, 2.75, 3.0) HEAs samples.

Parameters	Value
Laser power (W)	200
Scanning speed (mm/s)	400
Layer thickness (μm)	20
Hatching space (mm)	0.08

Results

Structures and formability

The XRD results of SLMed $AlCrCuFeNi_x$ HEAs with different contents of Ni are shown in Fig. 2. It can be found that the FCC phase is present as x increases to 2.0, which confirms the transition from BCC to FCC phase upon the addition of Ni. With the further increase of Ni, the relative volume fraction deduced from the XRD diffraction pattern for FCC phase obviously increases while that of BCC decreases. A moderate amount of BCC phase (~ 11%) is still captured by XRD as x increases to 3.0. This clearly confirms that the $AlCrCuFeNi_{3.0}$ HEA possesses dual-phase structures.

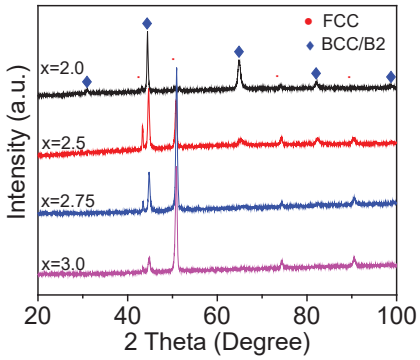

Fig. 2. XRD patterns of SLMed $AlCrCuFeNi_x$ HEAs with different contents of Ni.

The BSE images of SLMed $AlCrCuFeNi_x$ HEAs with various Ni content are shown in Fig.

3. Obviously, the micro-cracks are largely eliminated with the increase of Ni content. Only trace amounts of micro-cracks appear in $AlCrCuFeNi_{2.75}$ HEA. Finally, an increase to 3.0 Ni ($AlCrCuFeNi_{3.0}$) completely eliminates the micro-cracks. Additionally, EPMA analysis results illustrate that the five principal elements of SLMed samples are nearly uniform distribution in the sub-millimeter scale, verifying the homogeneous mixing of AlCrCuFeNi powders and Ni powders. Consequently, it can be concluded that a DP-HEA with good formability is successfully produced by SLM when x increases to 3.0. Then, the desired microstructures of $AlCrCuFeNi_{3.0}$ HEA are analyzed in detail in the following.

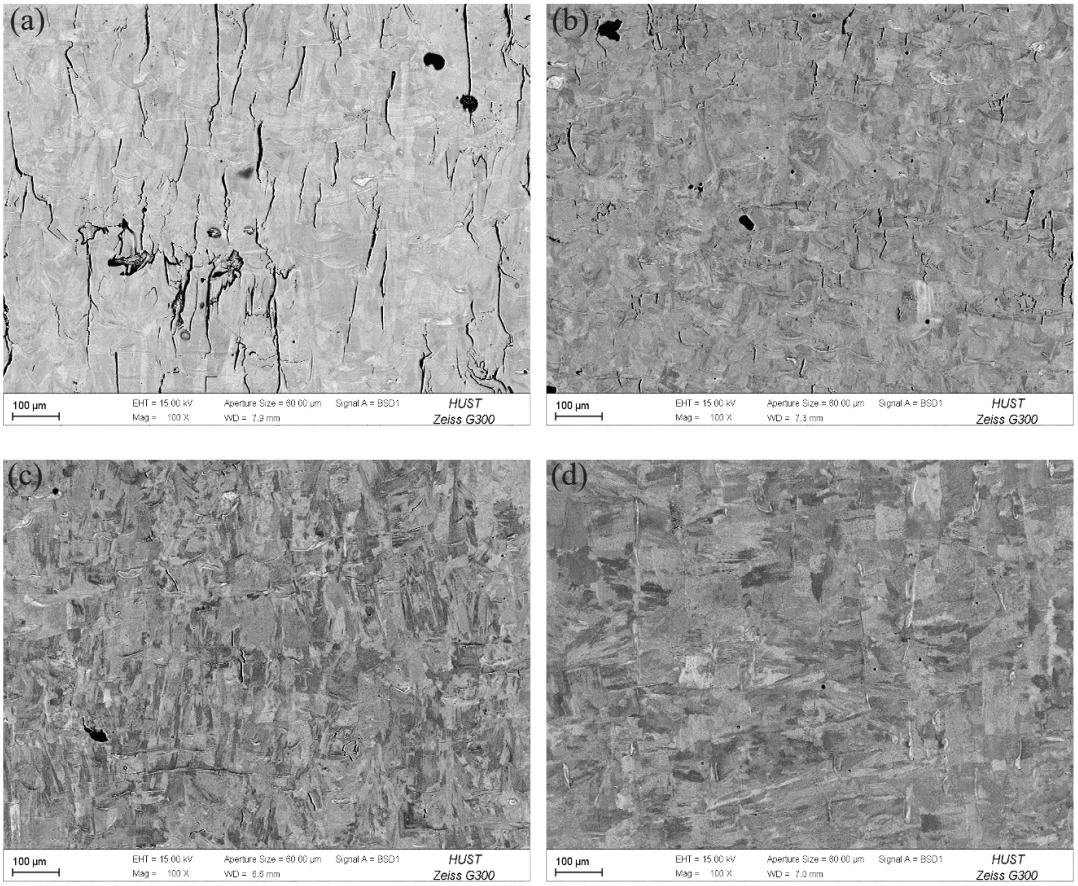

Fig. 3. Backscattered electron images of SLMed $AlCrCuFeNi_x$ HEAs: (a) x=2.0; (b) x=2.5; (c) x=2.75; (d) x=3.0.

Microstructures

Fig. 4 (a-b) shows the SEM images of SLMed $AlCrCuFeNi_3$ HEA along the building direction. Approximately equiaxed grains with different contrast are clearly observed (Fig. 4 (a)). Also, multiple ultrafine lamellar or cellular structures appear within the near-equiaxed grains. Meanwhile, the lamellar and cellular structures are usually interrupted at the grain boundaries, maybe contributing to the formation of near-equiaxed grains. Fig. 4 (b) shows the enlarged views of tiny lamellar structure. A large number of nano-precipitates with the mean size about 10 nm are present and distribute uniformly between the lamellar structures or cellular structures.

The bright-field TEM images further confirm the nano-sized lamellar and cellular structures of the SLMed $AlCrCuFeNi_{3.0}$ HEA, as depicted in Fig. 4 (c) and (d), respectively.

The selected area diffraction pattern (SADP) (the inset) in Fig. 4 (c) corresponding to the red circled region (Fig. 4 (c)) indicates the presence of disordered FCC phase. The clear superlattice spots marked by yellow circles in the SADP (the inset) in Fig. 4 (d) confirms that the blue circled region (Fig. 4 (c)) is ordered BCC (B2) phases. It was frequently reported that the strong negative mixing enthalpy of Al-Ni pair contributes to the formation of ordered B2 phase [22,23]. Meanwhile, the average thickness of FCC (~ 0.49 μm) in the lamellar regions is greater than that of the B2 phase (~ 0.14 μm). Similarly, the cellular structures shown in Fig. 4 (d) belong to the FCC phases, while the narrow bright regions around the cellular boundaries belong to the B2 phases. The average diameter of these cellular structures is about 0.65 μm. Additionally, the dislocations appear to be emitted from the FCC/B2 phase boundaries and then patterned into the lamellar and cellular structures. But due to more dislocation slip systems in FCC structure than in BCC structure, the lamellar and cellular structures are observed to contain profuse dislocation networks in FCC phases, with relatively clean interiors of B2 phases. From the above, it can be concluded that the ultrafine lamellar regions consist of FCC and B2 lamellae, and the cellular non-lamellar regions compose of FCC cells with the B2 phases surrounded. Similar cellular structures were also discovered in laser additively manufactured 316L stainless steel [24].

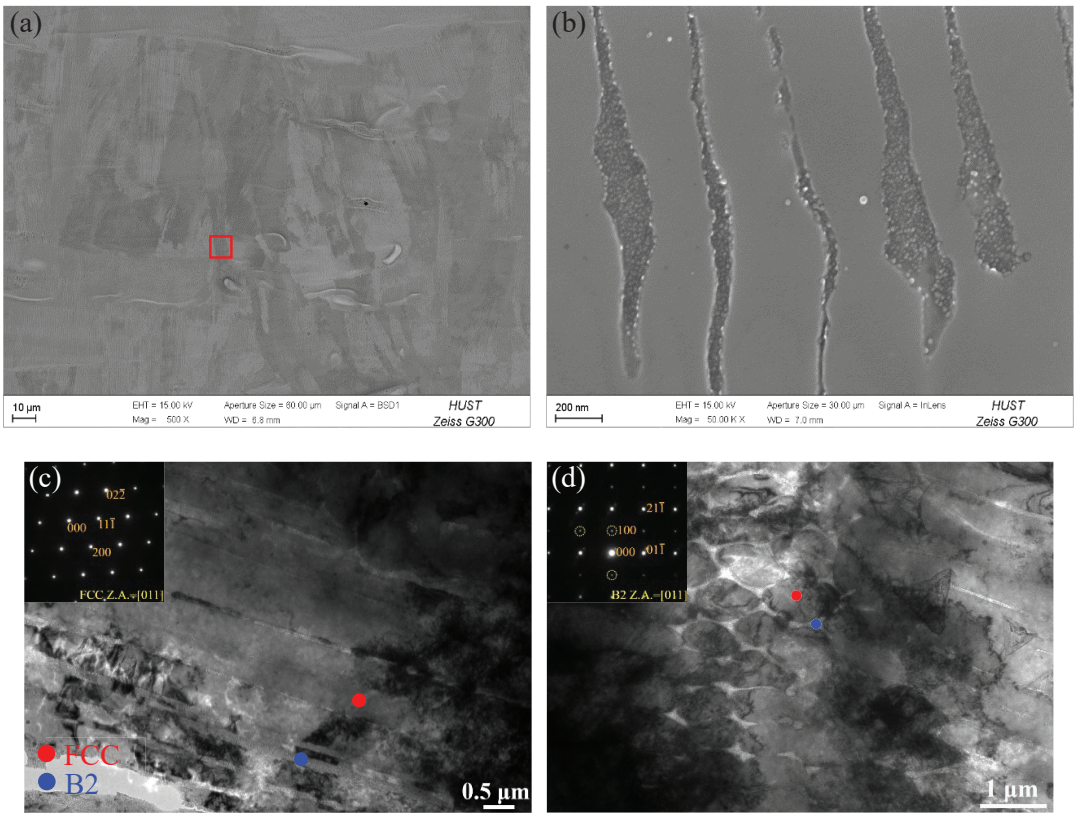

Fig. 4. (a) SEM images along the building direction; (b) Enlarged view of lamellar structures marked by red box in (a); (c) and (d) Bright-field TEM micrographs along the building direction; The insets SADPs correspond to the disordered FCC and ordered BCC (B2) phases, respectively. The zone axes (Z.A.) of FCC and B2 phases are [011] and [011], respectively.

The scanning transmission electron microscopy (STEM) micrograph at high magnification is shown in Fig. 5 (a). Notably, the B2 lamellae contain profuse nano-precipitates, as observed by SEM. No secondary phases are discovered in the FCC lamellae. STEM-EDS elemental distribution maps (Fig. 5 (b)) of the yellow boxed region reveal that the B2 lamellae are

enriched in Al and Cu, while the FCC lamellae are rich in Cr and Fe but depleted in Al and Cu elements. Also, the nano-precipitates are enriched in Cr. Such Cr-rich nano-precipitates embedded in B2 phases are first discovered in $AlCrCuFeNi_{3.0}$ HEA although similar findings were reported in other HEAs [23,25,26].

Fig. 5 (c) shows the high-resolution TEM (HRTEM) image of a nano-precipitate inside B2 phase with [001] zone axis. The nano-precipitate with a diameter of about 10 nm is marked by the red dotted box. The Fast-Fourier-Transformation (FFT) pattern in the inset demonstrates that the nano-precipitates inside B2 phase are disordered BCC (A2) structures, then the matrix of the blue circled regions in Fig. 4 (c) and (d) should be the ordered BCC (B2) phase. Thus, it can be deduced that BCC phases are spinodally decomposed into a mixture of B2 phase plus A2 phase during SLM [10,23].

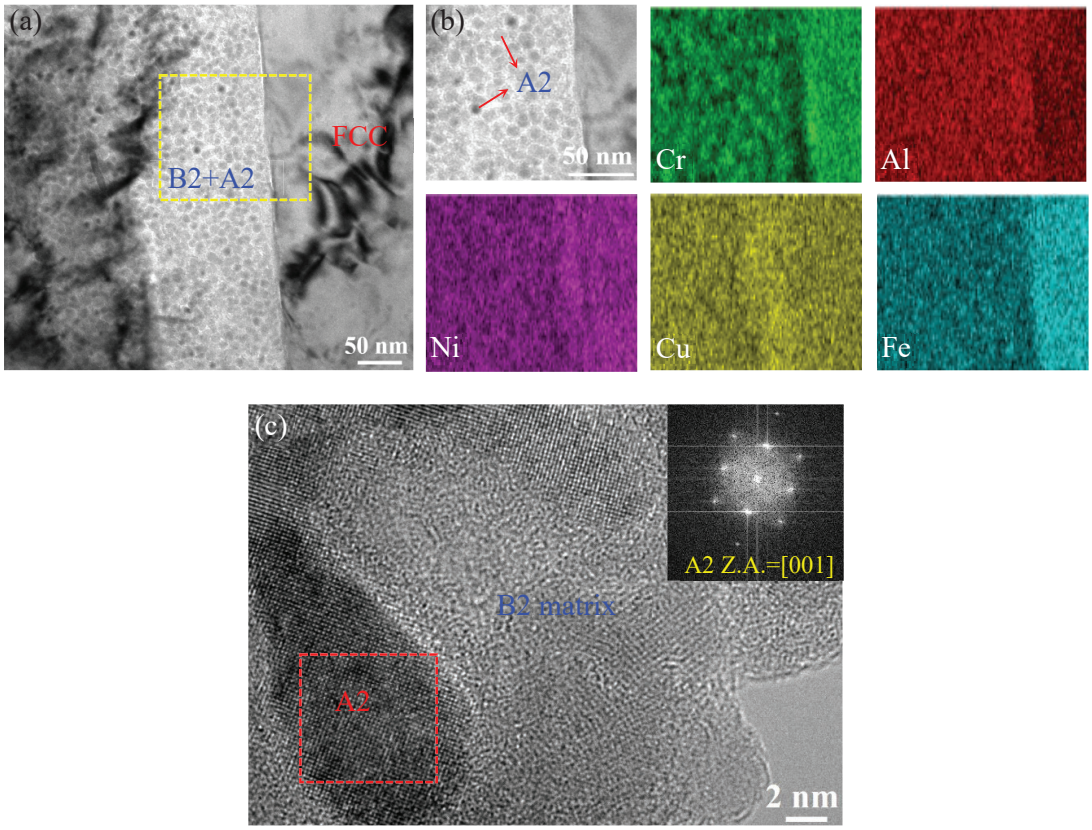

Fig. 5. (a) High magnification STEM image; (b) STEM-EDS maps of the yellow boxed region in (a); (c) HRTEM micrograph of a nano-precipitate inside B2 phase. Inset shows the FFT pattern of the red boxed region corresponding to A2 nano-precipitate.

The typical microstructure analyzed by EBSD for the SLMed $AlCrCuFeNi_{3.0}$ HEA is shown in Fig. 6 (a-b). Similarly, the grains under EBSD also present a near-equiaxed shape rather than a conventional columnar feature according to the inverse pole figure (IPF) in Fig. 6 (a). Meanwhile, a continuous variation of color and thus the change of orientation is clearly detected within one single grain, demonstrating that the near-equiaxed grains are filled with multiple ultrafine sub-structures. The GB map in Fig. 6 (b) shows that a significant fraction (~ 33.2% of total GBs) of low-angle grain boundaries (LAGBs, 2–15°) marked by white lines are detected within the near-equiaxed grains.

Fig. 6 (c-d) show the microstructural characteristic within one single grain at a higher magnification. It can be observed that the FCC (red) and B2 (blue) phases in alternating lamellar morphology are indexed in EBSD phase map at the nanoscale (Fig. 6 (c)). These are in fairly good accordance with the results observed from TEM. Based on the EBSD phase map, the volume fraction of FCC and B2 phases is calculated to be about 89.2% and 10.4%, respectively. The corresponding kernel average misorientations (KAMs) marked as rainbow ranging from 0° to 2° are illustrated in Fig. 6 (d). Local misorientations across lamellar structures are clearly present, demonstrating the existence of high lattice distortions, particularly in the vicinity of FCC/B2 phase boundaries. The dislocation multiplication and accumulation induced by rapid solidification may significantly contribute to the high lattice distortion.

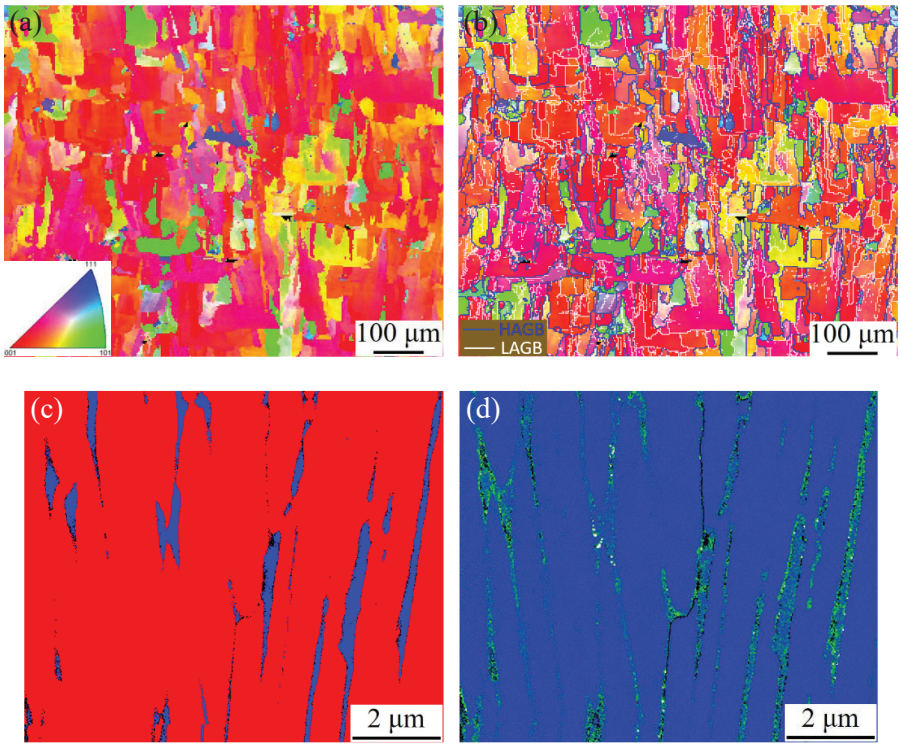

Fig. 6. (a) EBSD IPF map; (b) EBSD image quality (IQ) map with HAGBs (blue lines) and LAGBs (white lines) superimposed; (c) Phase map of magnified lamellar structures and (d) corresponding KAM map.

Based on the above analyzation, it can be concluded that the SLMed $AlCrCuFeNi_{3.0}$ HEA exhibits remarkably heterogeneous microstructures, both structural and chemical, including micron-sized near-equiaxed grains, nanoscale lamellar or cellular dual-phase structures, LAGBs, dislocations, nano-precipitates, and segregated elements (such as Cr, Al, and Cu). That is, the microstructure presents a multi-scale feature, nearly spanning from nanometre to sub-millimeter. The particular interests are the profuse A2 nano-precipitates embedded in B2 phases, as well as the solidification nanoscale lamellar or cellular dual-phase structure. These are scarcely observed in other reported SLMed HEAs [9-16].

Mechanical properties

Fig. 7 shows the tensile mechanical properties of SLMed $AlCrCuFeNi_x$ (x=2.0, 2.5, 2.75, 3.0) HEAs. Due to the existence of many micro-cracks, the properties of $AlCrCuFeNi_x$ (x=2.0, 2.5) HEAs are poor. However, the $AlCrCuFeNi_3$ HEA exhibits the best combination of the

ultimate tensile strength (~ 957 MPa) and ductility (~ 14.3%). Comparing the strength and elongation of selected HEAs, the synthetic mechanical properties of SLMed $AlCrCuFeNi_3$ HEA are superior to other SLMed HEAs [9,12-16], as-cast and cold-rolled plus annealed AlCrCuFeNi HEA system [27].

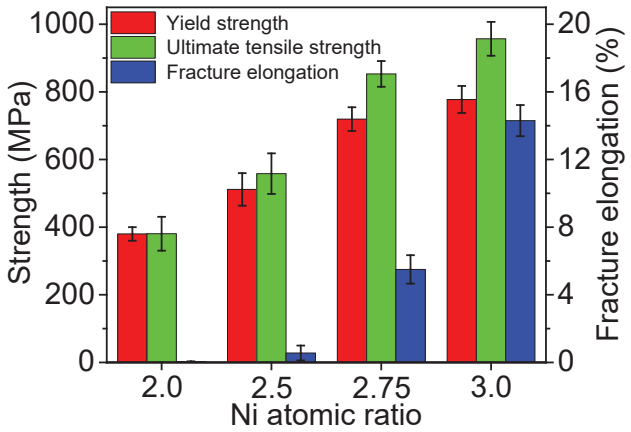

Fig. 7. Tensile mechanical properties of SLMed $AlCrCuFeNi_x$ (x=2.0, 2.5, 2.75, 3.0) HEAs.

It is considered that each element in HEA can be acted as solute atoms [1]. This can trigger a huge Cottrell atmosphere in the dislocation field, thus locking the dislocation [28]. Then, large drag forces on dislocations will be induced by abundant solutes atoms, and more tensile forces are necessary to make the dislocation free from this atmosphere. Consequently, the tensile stress significantly increases. Once the applied forces become sufficiently large, dislocations will escape from the lock of Cottrell atmosphere and move to the next obstacle with small stress. Additionally, the profuse highly coherent A2 nano-precipitates can effectively pin and drag dislocations in terms of the Orowan mechanism [26], thereby largely strengthening the B2 phase. Therefore, similar to the solute atoms, the profuse coherent A2 nano-precipitates can also serve as the obstacles of hindering moving dislocations. The continually pinning and unpinning of dislocations lead to the high ultimate tensile strength.

Additionally, it has been reported that the pronounced strengthening in heterogeneous materials is ascribed to the effect of back stress [19,21]. First, both FCC and B2 lamellas experience elastic deformation in a similar manner. Then, the hard B2 lamellas continue to elastically deform when the soft FCC lamellas start deforming plastically. The A2 precipitation strengthening makes the B2 lamellas harder to be deformed, aggravating the incompatibility of deformation. Thus, geometrically necessary dislocations (GNDs) are needed to accommodate this deformation incompatibility [29]. The accumulated GNDs can result in distinctly strengthening of the soft FCC lamellas through cross-slip mechanisms and forest hardening. Consequently, the yield strength is significantly improved. Finally, both FCC and B2 lamellas undergo plastically deforming, but the soft FCC lamellas are subjected to severer deformation, introducing strain partitioning [30]. As a result, strain gradients are built up near the FCC/B2 interfaces. The strain gradient increases with the strain partitioning increasing, thereby generating distinct back stress strengthening. The back stress strengthening is believed to prevent early local necking and then enhances the strength and ductility [29].

Similarly, the soft FCC cells with the hard B2 phases surrounded can produce profuse boundaries separating domains with different hardness. Consequently, a high density of GNDs will pile up at the FCC/B2 phase boundaries, which is particularly favorable to induce significant back stress strengthening. Moreover, the back stress, in turn, results in strain

repartitions and a change of internal stresses, which may result in a high flow stress. However, further studies are needed to verify this possible mechanism. In conclusion, the lamellar or cellular dual-phase microstructures featured by a mixture of soft FCC and hard B2 phases exhibit a nano-scale structural hierarchy, which leads to the high ultimate tensile strength and good tensile ductility of SLMed $AlCrCuFeNi_3$ HEA.

Conclusions

In summary, (FCC+BCC) DP-HEAs are first fabricated by the SLM technique. The SLMed $AlCrCuFeNi_3$ HEA exhibits heterogeneous microstructures, thus producing high strength and good ductility simultaneously. The feasibility of SLM additive manufacturing technique to prepare $AlCrCuFeNi_x$ (x=2.0, 2.5, 2.75, 3.0) DP-HEAs is explored. It is revealed that Ni addition favors the formation of FCC phases and improves the formability. The Cottrell atmosphere effect, A2 precipitation hardening and back stress strengthening induced by heterogeneous microstructures contribute to the high ultimate tensile strength (~ 957 MPa) and good ductility (~ 14.3 %) of SLMed $AlCrCuFeNi_{3.0}$ HEA.

Acknowledgments

This work was supported financially by the Pre-research Fund Project of Ministry of Equipment and Development of China (No. 61409230301), and the Fundamental Research Funds for the Central Universities through Program No.2019kfyXMPY005 and No.2019kfyXKJC042.

References

[1] J.W. Yeh, S.K. Chen, S.J. Lin, et al. Nanostructured high entropy alloys with multiple principal elements: novel alloy design concepts and outcomes, Adv Eng Mater. 6(5) (2004) 299–303.

[2] B. Gludovatz, A. Hohenwarter, D. Catoor, E.H. Chang, E.P. George, R.O. Ritchie, A fracture-resistant high-entropy alloy for cryogenic applications, Science. 345 (2014) 1153–1158.

[3] L.R. Owen, E.J. Pickering, H.Y. Playford, et al. An assessment of the lattice strain in the CrMnFeCoNi high-entropy alloy, Acta Mater. 122 (2017) 11–18.

[4] Z. Li, K.G. Pradeep, Y. Deng, et al. Metastable high-entropy dual-phase alloys overcome the strength-ductility trade off, Nature. 534 (2016) 227–230.

[5] T. Yang, Y.L. Zhao, Y. Tong, Z.B. Jiao, J. Wei, J.X. Cai, X.D. Han, D. Chen, A. Hu, J.J. Kai, K. Lu, Y. Liu, C.T. Liu, Multicomponent intermetallic nanoparticles and superb mechanical behaviors of complex alloys, Science. 362 (2018) 933–937.

[6] T. Bhattacharjee, I.S. Wani, S. Sheikh, I.T. Clark, T. Okawa, S. Guo, P.P. Bhattacharjee, N. Tsuji, Simultaneous Strength-Ductility Enhancement of a Nano-Lamellar $AlCoCrFeNi_{2.1}$ Eutectic High Entropy Alloy by Cryo-Rolling and Annealing, Sci. Rep. 8 (2018) 3276.

[7] B. Gwalani, V. Soni, D. Choudhuri, M. Lee, J.Y. Hwang, S.J. Nam, H. Ryu, S.H. Hong, R. Banerjee, Stability of ordered L12 and B2 precipitates in face centered cubic based high entropy alloys - $Al_{0.3}CoFeCrNi$ and $Al_{0.3}CuFeCrNi_2$, Scr. Mater. 123 (2016) 130–134.

[8] Z.M. Wang, K. Guan, M. Gao, X.Y. Li, X.F. Chen, X.Y. Zeng, The microstructure and mechanical properties of deposited-IN718 by selective laser melting, J. Alloy Compd. 513 (2012) 518–523.

[9] P.F. Zhou, D.H. Xiao, Z. Wu, X.Q. Ou, $Al_{0.5}FeCoCrNi$ high entropy alloy prepared by selective laser melting with gas-atomized pre-alloy powders, Mater. Sci. Eng. A. 739

(2019) 86–89.
[10] S.C. Luo, P. Gao, H.C. Yu, J.J. Yang, Z.M. Wang, X.Y. Zeng, Selective laser melting of an equiatomic AlCrCuFeNi high-entropy alloy: Processability, non-equilibrium microstructure and mechanical behavior, J. Alloys Compd. 771 (2019) 387–397.
[11] P. D. Niu, R. D. Li, T. C. Yuan, S. Y. Zhu, C. Chen, M. B. Wang, L. Huang, Microstructures and properties of an equimolar AlCoCrFeNi high entropy alloy printed by selective laser melting, Intermetallics. 104 (2019) 24–32.
[12] Y. Brif, M. Thomas, I. Todd, The use of high-entropy alloys in additive manufacturing, Scr. Mater. 99 (2015) 93–96.
[13] W.Q. Wu, R. Zhou, B.Q. Wei, S. Ni, Y. Liu, M. Song, Nanosized precipitates and dislocation networks reinforced C-containing CoCrFeNi high-entropy alloy fabricated by selective laser melting, Mater. Charact. 144 (2018) 605–610.
[14] R. Zhou, Y. Liu, C.S. Zhou, S.Q. Li, W.Q. Wu, M. Song, B. Liu, X.P. Liang, P.K. Liaw, Microstructures and mechanical properties of C-containing FeCoCrNi high-entropy alloy fabricated by selective laser melting, Intermetallics. 94 (2018) 165–171.
[15] Z.G. Zhu, Q.B. Nguyen, F.L. Ng, X.H. An, X.Z. Liao, P.K. Liaw, S.M.L. Nai, J. Wei, Hierarchical microstructure and strengthening mechanisms of a CoCrFeNiMn high entropy alloy additively manufactured by selective laser melting, Scr. Mater. 154 (2018) 20–24.
[16] R.D. Li, P.D. Niu, T.C. Yuan, P. Cao, C. Chen, K.C. Zhou, Selective laser melting of an equiatomic CoCrFeMnNi high-entropy alloy: Processability, non-equilibrium microstructure and mechanical property, J. Alloys Compd. 746 (2018) 125–134.
[17] S. Guo, C. Ng, J. Lu, C.T. Liu, Effect of valence electron concentration on stability of fcc or bcc phase in high entropy alloys, J. Appl. Phys. 109 (2011) 103505.
[18] T. Yang, Y.L. Zhao, W.H. Liu, J.H. Zhu, J.J. Kai, C.T. Liu, Y.L. Zhao, W.H. Liu, J.H. Zhu, J.J. Kai, C.T. Liu, Ductilizing brittle high-entropy alloys via tailoring valence electron concentrations of precipitates by controlled elemental partitioning, Mater. Res. Lett. 10 (2018) 600–606.
[19] Z.Q. Fu, B.E. MacDonald, Z.M. Li, Z.F. Jiang, W.P. Chen, Y.Z. Zhou, E.J. Lavernia, Engineering heterostructured grains to enhance strength in a single-phase high-entropy alloy with maintained ductility, Mater. Res. Lett. 6 (2018) 634–640.
[20] S. Shukla, D. Choudhuri, T.H. Wang, K.M. Liu, R. Wheeler, S. Williams, B. Gwalani, R.S. Mishra, Hierarchical features infused heterogeneous grain structure for extraordinary strength-ductility synergy, Mater. Res. Lett. 6 (2018) 676–682.
[21] J. Su, D. Raabe, Z.M. Li, Hierarchical microstructure design to tune the mechanical behavior of an interstitial TRIP-TWIP high-entropy alloy, Acta Mater. 163 (2019) 40–54.
[22] C. Li, M. Zhao, J.C. Li, B2 structure of high-entropy alloys with addition of Al. J Appl Phys. 104 (2008) 113504.
[23] J.Y. He, W.H. Liu, H. Wang, Y. Wu, X.J. Liu, T.G. Nieh, Z.P. Lu, Effects of Al addition on structural evolution and tensile properties of the FeCoNiCrMn high-entropy alloy system, Acta Mater. 62 (2014) 105–113.
[24] Y.M. Wang, T. Voisin, J.T. McKeown, J. Ye, N.P. Calta, Z. Li, Z. Zeng, Y. Zhang, W. Chen, T.T. Roehling, R.T. Ott, M.K. Santala, P.J. Depond, M.J. Matthews, A. V. Hamza, T. Zhu, Additively manufactured hierarchical stainless steels with high strength and ductility, Nat. Mater. 17 (2018) 63–70.
[25] D. Choudhuri, B. Gwalani, S. Gorsse, C. V. Mikler, R. V. Ramanujan, M. A. Gibson, R. Banerjee, Change in the primary solidification phase from fcc to bcc-based B2 in high entropy or complex concentrated alloys, Scr. Mater. 127 (2017) 186–190.
[26] X. Gao, Y. Lu, B. Zhang, N. Liang, G. Wu, G. Sha, J. Liu, Y. Zhao, Microstructural origins of high strength and high ductility in an $AlCoCrFeNi_{2.1}$ eutectic high-entropy

alloy, Acta Mater. 141 (2017) 59–66.
[27] S.G. Ma, J.W. Qiao, Z.H. Wang, H.J. Yang, Y. Zhang, Microstructural features and tensile behaviors of the $Al_{0.5}CrCuFeNi_2$ high-entropy alloys by cold rolling and subsequent annealing, Mater. Des. 88 (2015) 1057–1062.
[28] A.H. Cottrell, B.A. Bilby, Dislocation theory of yielding and strain ageing of iron, Proc Phys Soci. Section A. 62 (1949) 49.
[29] E. Ma, T. Zhu, Towards strength–ductility synergy through the design of heterogeneous nanostructures in metals, Mater. Today. 20 (2017) 323–331.
[30] M.X. Yang, Y. Pan, F.P. Yuan, Y.T. Zhu, X.L. Wu, Back stress strengthening and strain hardening in gradient structure, Mater. Res. Lett. 4 (2016) 145–151.